



1 Microphysical modelling of aerosol scavenging by different types of clouds.

2 Description and validation of the approach

3
4 Pascal Lemaître¹, Arnaud Querel², Alexis Dépée¹, Alice Guerra Devigne¹, Marie Monier^{3,4}, Thibault Hiron³, Chloé Soto Minguez¹, Andrea Flossmann^{3,4}

5
6 [1] { Institut de Radioprotection et de Sécurité Nucléaire (IRSN), PSN-RES/SCA/LPMA, F-91400, Saclay, France}

7 [2] { Institut de Radioprotection et de Sécurité Nucléaire (IRSN), PSE-SANTE/SESUC/BMCA, F-92260, Fontenay-aux-Roses, France}

8 [3] {Clermont University, Blaise Pascal University, Physical Meteorology Laboratory, Clermont-Ferrand, France}

9 [4] {CNRS, INSU, UMR 6016, LaMP, Aubière, France}

10 Correspondence to: P. Lemaître (pascal.lemaître@irsn.fr & arnaud.querel@irsn.fr)

11 12 **Short abstract**

13 A new in-cloud scavenging scheme is proposed. It is based on a microphysical model of cloud formation and may be applied to long-distance atmospheric
14 transport models (>100 km) and climatic models. This model is established for the two most extreme precipitating cloud types, in terms of both relative
15 humidity and vertical extension: cumulonimbus and stratus.

16 17 **Abstract**

18 With dry deposition and below-cloud scavenging, in-cloud scavenging is one of the three components of aerosol transfer from the atmosphere to the ground.
19 There is no experimental validation of in-cloud particle scavenging models for all cloud types that is not impacted by uncertainties concerning below-cloud
20 scavenging. In this article, the choice was made to start with a recognised and validated microphysical cloud formation model (DESCAM) to extract a scheme
21 of aerosol scavenging by clouds, valid for different cloud types. The resulting model works for the two most extreme precipitation clouds: from
22 cumulonimbus to stratus. It is based on data accessible a priori from Numerical Weather Prediction (NWP) outputs, i.e., the intensity of the rain and the
23 relative humidity in the cloud. The diagnostic of the altitude of the cloud base proves to be a key parameter, and accuracy in this regard is vital. This new in-
24 cloud scavenging scheme can be used by long-distance (> 100 km) Atmospheric Transport Models (ATMs) or Global Climate Models (GCMs).

25 26 **Introduction**

27
28 Clouds are an essential component of the troposphere. They play a central role in meteorological forecasting and in the water cycle on the planet (Zhang *et al.*,
29 2020). Similarly, by interacting with solar radiation, they make a significant contribution to the terrestrial radiation balance (Twomey, 1974; Wang and
30 Su, 2013). Moreover, they are often cited as one of the main sources of uncertainty in climate prediction models (Bony and Dufresne, 2005; Palmer, 2014).
31 They can seriously disrupt air traffic, and even produce aircraft crashes (e. g. Air France flight 447 Rio-Paris air disaster).

32 By scavenging aerosols, they will contribute to improving air quality (Leaith *et al.*, 1987; Sievering *et al.*, 1984), but also to impacting soil pollution, through
33 the deposition of atmospheric pollutants via precipitation (Clark and Smith, 1988; Flossmann, 1998). In case of severe accident, radioactive aerosol particles
34 might be released into the troposphere (De Cort, 1998 ; Baklanov and Sørensen, 2001 ; Adachi *et al.*, 2013). When radionuclides are emitted into the
35 environment, it is essential, in order to protect populations, to jointly assess the concentrations of radioactive aerosols in the atmospheric boundary layer,
36 as well as their transfer to the ground. Thus, during the accidental phase, it is possible to accurately assess the exposures of populations, both by inhalation
37 and by ingestion (Mathieu *et al.*, 2004; Quélo *et al.*, 2007; Quérel *et al.*, 2012).

38 In nature, deposition of aerosols (and therefore a fortiori of particulate radionuclides) on the ground consists of the contribution of dry deposition and of
39 wet deposition (Slinn 1977). Dry deposition is approximately 1000 times less effective than wet deposition, but is the only mechanism operating when there
40 is no precipitation. To date, there are still many uncertainties about the modelling of these two deposition pathways (Petroff *et al.*, 2008).

41 Flossmann (1998) used the DESCAM model (Flossmann *et al.*, 1985, 1987, 1988) to assess that, for a droplet from a convective cloud, about 70% of the mass
42 of particles the droplet contains when deposited on the ground was incorporated into the droplet in the cloud. This result is consistent with the
43 measurements in the environment of Laguionie *et al.*, (2014), which estimate the cloud to be 60% responsible for the total downwash of particles.

44 Our objective in this article is to establish theoretically a scavenging coefficient applicable to clouds. The fact is that scavenging by clouds is much more
45 delicate to model than scavenging by rain, under the cloud. Rain scavenging is only controlled by a single microphysical mechanism: collection by raindrops



46 (Kerker and Hampl, 1974; Beard, 1974; Grover *et al.*, 1977; Wang and Pruppacher, 1977; Lai *et al.*, 1978; Pranesha and Kamra, 1996; Vohl *et al.*, 1999; Quérel
 47 *et al.*, 2014; Lemaitre *et al.*, 2017), whereas cloud scavenging encompasses a set of mechanisms which will firstly make it possible to incorporate aerosols
 48 into the cloud droplets (activation, collection, ice nucleation, collection by crystals) then, secondly, to convert a fraction of the cloud hydrometeors into
 49 raindrops (condensation, coalescence, Bergeron effects). Only after raindrops have been deposited on the ground is the atmosphere washed out and, by
 50 the same token, the soil contaminated. Furthermore, the majority of atmospheric transport models use significantly different schemes to model scavenging
 51 by cloud and by rain. Quérel *et al.*, 2021 summarised all these models in Table 3 of their article.

52 Therefore, to theoretically assess cloud scavenging, it seems wise to use a cloud formation model such as DESCAM (DEtailed SCAvenging Model). This model,
 53 developed by Andrea Flossmann and her group since the mid-80s (Flossmann *et al.*, 1985; Flossmann, 1998; Monier *et al.*, 2006; Leroy *et al.*, 2007; Planche
 54 *et al.*, 2007; Flossmann and Wobrock, 2010; Hiron and Flossmann, 2015; Dépée, 2019), makes it possible, through a detailed microphysical description, to
 55 model clouds from their formation through to precipitation, and to monitor the aerosols and what becomes of them once incorporated into the droplets.
 56 In this article, we will show how, using a model like DESCAM, it is possible to theoretically calculate a scavenging coefficient in the cloud, on the scale of the
 57 cloud system. We will apply this approach to two extreme types of cloud: a cumulonimbus (CCOPE, Dye *et al.*, 1986) and a stratus (Zhang *et al.*, 2004). This
 58 approach will then be compared to the models derived from the deposits observed following the Fukushima nuclear accident (Leadbetter *et al.*, 2015; Querel
 59 *et al.*, 2021). Finally, in the last part, a theoretical scheme of the scavenging coefficient, applicable to any type of cloud, will be proposed. Let us begin by
 60 considering some elements of theoretical context and some definitions.

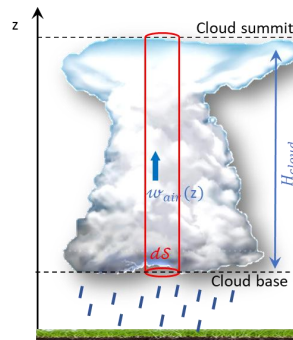
61 1. Definitions and theoretical context

62 1.1. Definition of cloud scavenging

63 In large range transport models, the description of scavenging shall remain simple, the operational scientific community models it through a parametrisation
 64 involving the cloud scavenging coefficient (Λ_{cloud}). It is defined as the fraction of pollutants that is transferred from the atmosphere to precipitation (then
 65 to the ground) per unit of time. In this article, we will focus on pollutants carried by aerosols (and not gaseous pollutants). The scavenging coefficient is
 66 therefore defined spectrally thus:

$$67 \quad \left. \frac{dN(d_{ap})}{N(d_{ap})} \right|_{cloud} = \left. \frac{dM(d_{ap})}{M(d_{ap})} \right|_{cloud} = -\Lambda_{cloud}(d_{ap}) \cdot dt \quad \text{Equation 1}$$

68 In this equation $N(d_{ap})$ and $M(d_{ap})$ are respectively the concentrations in number and in mass of aerosols of diameter d_{ap} per unit of air volume;
 69 likewise, $dN(d_{ap})$ and $dM(d_{ap})$ are respectively the variations in concentration in number and in mass of aerosols of diameter d_{ap} , in relation to their
 70 transfer into precipitation, per unit of time. The idea is to apply this definition to an elementary volume of cloud (volume outlined in red in Figure 1). This
 71 volume is bounded at its base by an arbitrary section (dS) aligned with the base of the cloud, with this volume extending vertically to the cloud summit.



72
 73 Figure 1. Definition of the scavenging coefficient at the scale of a cloud

74
 75 In this elementary cloud volume, it is elementary to calculate the variation in the average mass concentration of aerosols of diameter d_{ap} , in relation to
 76 their transfer into precipitation:

$$77 \quad dM(d_{ap}) = - \frac{\phi_{ap,precip}(d_{ap}) \cdot dS \cdot dt}{dV_{cloud}} \quad \text{Equation 2}$$

78
 79
 80 In this equation, $\phi_{ap,precip}(d_{ap})$ is the mass flow of dry particles of diameter (d_{ap}) leaving the cloud via precipitation (solids and liquids), and dV_{cloud} is the
 81 elementary volume of cloud considered ($dV_{cloud} = H_{cloud} \cdot dS$).



$$\Lambda_{cloud}(d_{ap}) = - \frac{1}{dt} \frac{d\mathcal{M}(d_{ap})}{\langle \mathcal{M}(d_{ap}) \rangle_{cloud}} \Big|_{cloud} = \frac{\phi_{ap, precip}(d_{ap})|_{dS}}{\langle \mathcal{M}(d_{ap}) \rangle_{cloud} \cdot H_{cloud}} \quad \text{Equation 3}$$

82 In this equation, $\langle \mathcal{M}(d_{ap}) \rangle$ is the average mass concentration (over the thickness of the cloud) of dry particles of diameter d_{ap} . Attention: $\langle \mathcal{M}(d_{ap}) \rangle$ is not
 83 the average concentration of interstitial aerosols in the cloud but the average concentration of particles, which includes, in addition to the interstitial
 84 aerosols, all the particles included in the droplets and potentially in the ice phase. Thus, if we are able to jointly determine $\langle \mathcal{M}(d_{ap}) \rangle$, $\phi_{ap, precip}$ as well
 85 as the thickness of the cloud H_{cloud} , it is possible to deduce a scavenging coefficient.

86 The average particle concentration is calculated, using Equation 4, by spatially averaging, over the entire thickness of the cloud, the concentrations of
 87 interstitial aerosols (of diameters d_{ap}) $\mathcal{M}_{int}(z, d_{ap})$, the concentrations of particles in the drops ($\mathbb{M}(z, d_{ap})$), and the concentrations in the ice phase
 88 ($\mathfrak{M}(z, d_{ap})$).

$$\langle \mathcal{M}(d_{ap}) \rangle = \frac{1}{H_{cloud}} \int_{cloud\ base}^{cloud\ summit} (\mathcal{M}_{int}(z, d_{ap}) + \mathbb{M}(z, d_{ap}) + \mathfrak{M}(z, d_{ap})) dz \quad \text{Equation 4}$$

89

90 Finally, in order to evaluate the mass flow of particles exiting the cloud at its base ($\phi_{ap, precip}(d_{ap})$), it is necessary to evaluate the cloud volume ($\mathcal{V}_{\mathcal{D}_{drop}}$)
 91 which contains all the droplets whose drop velocity $w_{\infty}(\mathcal{D}_{drop})$ is sufficient for them to pass through the section dS , during the time dt . Using the velocity
 92 composition law, we can deduce Equation 5.

$$\mathcal{V}_{\mathcal{D}_{drop}} = \max(0, w_{\infty}(\mathcal{D}_{drop}) - w_{air}(Z_{cloud\ base})). dS \quad \text{Equation 5}$$

93

94 In this equation, $w_{air}(Z_{cloud\ base})$ is the velocity of the air parcel at the base of the cloud. By convention, w_{air} is positive for an updraft and negative for
 95 a downdraft.

96 It is then immediately possible to deduce the flow of particles passing dS through liquid precipitation:

$$\phi_{ap, rain}(d_{ap}) = \int_{\mathcal{D}_{droplet}=0}^{\infty} \max(0, w_{\infty}(\mathcal{D}_{drop}) - w_{air}(Z_{cloud\ base})) \cdot \mathbb{M}(z, d_{ap}, \mathcal{D}_{drop}) \cdot d\mathcal{D}_{drop} \quad \text{Equation 6}$$

97 In this equation, $\mathbb{M}(z, d_{ap}, \mathcal{D}_{drop})$ is the concentration of particles contained in the droplets and of dry diameter d_{ap} .

98 The same applies to solid precipitation $\phi_{ap, ice}(d_{ap})$:

$$\phi_{ap, ice}(d_{ap}) = \int_{d_{ice}=0}^{\infty} \max(0, w_{\infty}(d_{ice}) - w_{air}(Z_{cloud\ base})) \cdot \mathfrak{M}(z, d_{ap}, d_{ice}) \cdot d d_{ice} \quad \text{Equation 7}$$

99 By adding these two flows together, it is possible to deduce the total flow of particles (of diameter d_{ap}) exiting the cloud through all precipitation:

100

$$\phi_{ap, precip}(d_{ap}) = \phi_{ap, rain}(d_{ap}) + \phi_{ap, ice}(d_{ap}) \quad \text{Equation 8}$$

101

102 Thus, to theoretically evaluate the cloud scavenging coefficient, it is first and foremost essential to be able to evaluate its contours, but also to be able to
 103 determine the mass concentrations of particles in the droplets $\mathbb{M}(z, d_{ap}, \mathcal{D}_{drop})$, in the ice phase $\mathfrak{M}(z, d_{ice}, d_{ap})$, and in the interstitial aerosol $\mathcal{M}_{int}(z, d_{ap})$.

104 To evaluate the contours of the cloud, it seems necessary in the first instance to consider once again its definition.

105

1.2. What is a cloud? (how to define its boundaries?)

106 The World Meteorological Organization defines clouds as: "an aggregation of minute particles of liquid water or ice, or of both, suspended in the atmosphere
 107 and usually not touching the ground" (WMO, 2014). This definition would appear to be very inadequate for enabling the contours of a cloud to be
 108 determined. Clouds, although very commonly talked about in everyday life and subject to numerous scientific studies, have contours that remain very
 109 blurred. It is therefore always difficult to define them rigorously, and above all non-recursively. Spankuch *et al.*, (2022) further emphasised that, depending
 110 on the scope of the authors' expertise (meteorology, climate, satellite observations, airborne, from ground radars, or using microphysical models), these
 111 authors use significantly differing definitions and thresholds.

112 For example, Wood and Field, 2011 proposed criteria with respect to liquid water content (LWC), ice water content (IWC), or total concentrations in numbers
 113 of hydrometeors (droplets and crystals).



114 Hiron (2018) proposed separating cloud water and precipitation water based on the criterion of the size of hydrometeors (hydrometeors with a diameter of
 115 less than $64 \mu\text{m}$ are considered part of the cloud; larger than that are considered part of the rain); then, if the total cloud water content is greater than 0.1
 116 g/cm^3 , the air parcel is considered part of the cloud.

117 Other authors proposed contours based on relative humidity (Del Genio *et al.*, 1996) or total water content (TWC), whereas meteorologists and
 118 climatologists tend to prefer optical thickness (Sassen and Cho, 1992), each with arbitrarily established thresholds.

119 Although these definitions can be linked mathematically to each other, these relationships are most often highly non-linear. Therefore, in this article, our
 120 study will be at variance from these criteria, and we will examine the criteria that are most relevant for studying in-cloud scavenging and distinguishing it
 121 from below-cloud scavenging. This relevance will be analysed from two perspectives. Firstly, we consider a purely physical aspect and, secondly, a more
 122 pragmatic aspect linked rather to applicability in an atmospheric dispersion model dedicated to crisis management.

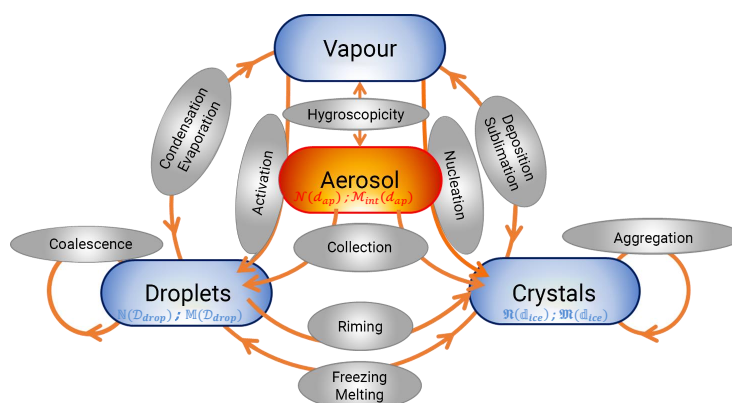
1.3. The DESCAM model

124 To simulate clouds of different types and theoretically evaluate their scavenging coefficient, it is necessary to have a model that makes it possible to simulate
 125 all the water phase changes, taking into account the catalyst role of aerosols in most of these state changes (activation, ice nucleation, etc.). It is also
 126 necessary to calculate the sink terms of interstitial aerosols (related to droplet collection or activation) and associate them with the source terms of particles
 127 in droplets and ice, in order to calculate the mass of particles in droplets ($\mathcal{M}(d_{\text{drop}})$) and in ice ($\mathcal{M}(d_{\text{ice}})$) throughout the simulation (Equation 6, Equation
 128 7).

129 The DESCAM model meets these specifications. This detailed microphysical model classifies droplets ($\mathcal{D}_{\text{drop}} \in [1 \mu\text{m}, 6.5 \text{mm}]$), ice ($\mathcal{d}_{\text{ice}} \in$
 130 $[1 \mu\text{m}, 6.5 \text{mm}]$), and aerosols ($d_{\text{ap}} \in [2 \text{nm}, 12.7 \mu\text{m}]$), each into 39 logarithmically distributed size classes. This makes it possible to explicitly monitor
 131 their respective particle size distributions $\mathcal{N}(\mathcal{D}_{\text{drop}})$, $\mathcal{N}(\mathcal{d}_{\text{ice}})$ and $\mathcal{N}(d_{\text{ap}})$, spatially and temporally. This model can be coupled with various dynamic models
 132 that allow consideration of atmospheric flows. In this article, we will only consider a dynamic called 1D1/2 (Asai and Kasahara, 1967), implemented in the
 133 DESCAM model by Monier, 2003. More realistic 3D dynamics (Clark and Hall, 1991) are implemented in DESCAM (Leroy 2007), but will not be considered in
 134 this article.

135 Description of the microphysical models modelled in DESCAM

136 All the microphysical processes considered in the DESCAM model are presented in Figure 2.



137

138 Figure 2. Modelling of microphysical processes in the DESCAM model.

139 In this figure, we can see the central role of aerosols in most water phase changes. The explicit resolution of all these microprocesses enables calculation of
 140 the particle size distributions of aerosols in each grid cell and at each time step (in number: $\mathcal{N}(d_{\text{ap}})$ (Equation 9) and in mass: $\mathcal{M}(d_{\text{ap}})$), as well as the
 141 particle size distributions of the droplets (in number $\mathcal{N}(\mathcal{D}_{\text{drop}})$, Equation 10) and of the ice (in number $\mathcal{N}(\mathcal{d}_{\text{ice}})$, Equation 11). In addition, in order to preserve
 142 the total mass of particles, the model also calculates two other quantities that are used to determine the masses of particles in droplets of diameter d_{drop}
 143 ($\mathcal{M}(\mathcal{D}_{\text{drop}})$), and in ice crystals of diameter d_{ice} ($\mathcal{M}(\mathcal{d}_{\text{ice}})$).

144



$$\frac{dN(d_{ap})}{dt} = \frac{dN(d_{ap})}{dt}\Big|_{d_{syn}} + \frac{dN(d_{ap})}{dt}\Big|_{coll} + \frac{dN(d_{ap})}{dS_{v,w}}\Big|_{Köhler} \frac{dS}{dt}\Big|_{d_{syn}} + \frac{dN(d_{ap})}{dt}\Big|_{act, deact}$$

Equation 9

145

$$\frac{dN(D_{drop})}{dt} = \frac{dN(D_{drop})}{dt}\Big|_{d_{syn}} + \frac{dN(D_{drop})}{dt}\Big|_{act, deact} + \frac{dN(D_{drop})}{dt}\Big|_{coal} + \frac{dN(D_{drop})}{dt}\Big|_{cond, vap} + \frac{dN(D_{drop})}{dt}\Big|_{riming} + \frac{dN(D_{drop})}{dt}\Big|_{frz, melt}$$

Equation 10

146

$$\frac{dN(\underline{d}_{ice})}{dt} = \frac{dN(\underline{d}_{ice})}{dt}\Big|_{d_{syn}} + \frac{dN(\underline{d}_{ice})}{dt}\Big|_{nucleation} + \frac{dN(\underline{d}_{ice})}{dt}\Big|_{frz, sub} + \frac{dN(\underline{d}_{ice})}{dt}\Big|_{agg} + \frac{dN(\underline{d}_{ice})}{dt}\Big|_{riming} + \frac{dN(\underline{d}_{ice})}{dt}\Big|_{frz, melt}$$

Equation 11

147

$$\frac{dM(D_{drop})}{dt} = \frac{dM(D_{drop})}{dt}\Big|_{d_{syn}} + \frac{dM(D_{drop})}{dt}\Big|_{act, deact} + \frac{dM(D_{drop})}{dt}\Big|_{coal} + \frac{dM(D_{drop})}{dt}\Big|_{cond, vap} + \frac{dM(D_{drop})}{dt}\Big|_{riming} + \frac{dM(D_{drop})}{dt}\Big|_{frz, melt}$$

Equation 12

148

$$\frac{dN(\underline{d}_{ice})}{dt} = \frac{dN(\underline{d}_{ice})}{dt}\Big|_{d_{syn}} + \frac{dN(\underline{d}_{ice})}{dt}\Big|_{nucleation} + \frac{dN(\underline{d}_{ice})}{dt}\Big|_{frz, sub} + \frac{dN(\underline{d}_{ice})}{dt}\Big|_a + \frac{dN(\underline{d}_{ice})}{dt}\Big|_{riming} + \frac{dN(\underline{d}_{ice})}{dt}\Big|_{frz, melt}$$

Equation 13

149

150

151 In these equations, apart from the index $(\Big|_{d_{syn}})$ which refers to the variations of each of the distributions due to transport by atmospheric flows, all other
 152 terms refer to each of the microphysical processes presented in Figure 2. For example, $(\Big|_{act, deact})$ refers to the activation and deactivation processes.

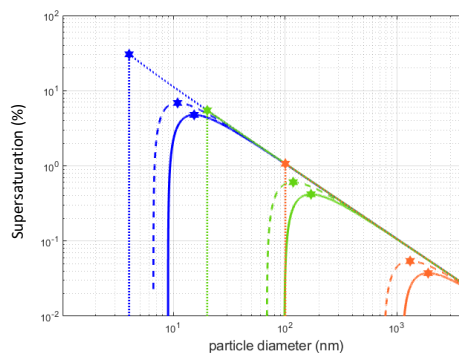
153 Concerning the cold microphysics (Figure 2), this simulation integrates homogeneous freezing mechanisms (i.e., which do not require aerosol contribution)
 154 and heterogeneous freezing mechanisms (for which aerosols act as a catalyst for phase change). For homogeneous freezing, we consider the parametrisation
 155 of Koop *et al.*, (2000) adapted to DESCAM by Monier *et al.*, (2006). To model heterogeneous ice nucleation, we consider all the mechanisms described by
 156 Vali *et al.*, (2015). The Biggs formula (1953) is used to describe immersion freezing and the model of Meyers *et al.*, (1992) for condensation and contact
 157 freezing, as well as deposition nucleation. All these mechanisms have recently been incorporated into the DESCAM model by Hiron and Flossmann, (2015).

158 The main mechanism responsible for the flow of particles exiting the cloud via precipitation ($\phi_{ap, precip}(d_{ap})$, Equation 3) is activation. The collection of
 159 aerosols by droplets is only second order (Flossmann and Wobrock, 2010; Dépée, 2019). In the DESCAM model, activation is modelled by the κ -Köhler theory
 160 (Petters and Kreidenweis, 2007). This model makes it possible to determine equilibrium vapour pressure in the vicinity of a droplet of diameter D_{drop} , as a
 161 function of the mass and type of solute (modelled by the κ value) it contains; and therefore the supersaturation for this particular droplet. For a given mass
 162 and chemical nature of the pristine dry particle, one can compute the corresponding supersaturations for given size of solution droplets. This curve has a
 163 unique maximum, called critical supersaturation (Figure 3). The diameter associated with this critical supersaturation is called the activation diameter.
 164 Aerosols with a diameter smaller than the activation diameter are brought into thermodynamic equilibrium with their environment by hygroscopicity, with
 165 aerosols of a diameter greater than the activation diameter being converted into droplets and growing by means of vapour diffusion (by condensation).

166 In the DESCAM code, the microphysical process of collection (i.e. the process by which, during falling, droplets encounter impact and capture interstitial
 167 aerosol particles), is modelled in Equation 12 by the term $\frac{dM(D_{drop})}{dt}\Big|_{coll}$ which is calculated by solving Equation 14. In this equation, the central term is the
 168 collection efficiencies $(E(d_{ap}, D_{drop}, \mathcal{RH}))$. This is calculated by the model developed and validated by Dépée (Dépée *et al.*, 2019; Dépée *et al.*, 2021, Part I;
 169 Dépée *et al.*, 2020, Part II).

$$\frac{dM(D_{drop})}{dt}\Big|_{coll} = \int_{d_{ap}=0}^{\infty} N(d_{ap}) \frac{\pi D_{drop}^2}{4} u_{\infty, droplet}(D_{drop}) E(d_{ap}, D_{drop}, \mathcal{RH}) \frac{\pi d_{ap}^3}{6} \rho_{ap} dd_{ap}$$

Equation 14



170

171 Figure 3. Thermodynamic equilibrium of an aerosol calculated as a function of particle diameter and nature of the initial dry particle. This
172 calculation is made using the κ -Köhler theory (for a temperature of 293 K and a surface tension between solution and air of $72 \times 10^{-3} \text{ N.m}^{-1}$).
173 (—): for an initial dry radius of the particles set at 4 nm aerosol; (---): initial dry radius set at 20 nm; (—): initial dry radius set at 100 nm. (···):
174 $\kappa = 0$ modelling an insoluble aerosol (totally hydrophobic); (- -): $\kappa = 0.61$ modelling an aerosol moderately hygroscopic as is $(\text{NH}_4)_2\text{SO}_4$ (—); κ
175 = 1.28 modelling a highly hygroscopic aerosol particle as is NaCl. *: critical supersaturations needed to activate the aerosol and convert it
176 into a cloud droplet

177

178 Note that Equation 6 and Equation 7, which we established in the first section of this article, are not directly calculable by the DESCAM model. This is because
179 the model makes an inventory of the mass of particles in the droplets and crystals according to the size of the hydrometeors ($M(D_{drop})$, Equation 12 and
180 $M(\mathbb{M}_{ice})$, Equation 13), but without memorising the size of the aerosols before their incorporation. The scavenging coefficients calculated in this article are
181 therefore averaged, in mass, over the particle size distribution of the aerosols. We will see in an article that follows on from this one that it is relatively
182 simple to calculate this scavenging coefficient spectrally, without modifying the model. In this article, we focus on validating this approach by applying it to
183 different types of clouds.

184

185 Modelling of atmospheric dynamics

186 As stated previously, in this article we have limited our study to the 1.5D Dynamic framework developed by Asai and Kasahara, (1967). This has been regularly
187 used (Monier *et al.*, 2005; Leroy *et al.*, 2006; Quérel *et al.*, 2014; Hiron & Flossmann, 2015) to study the microphysical processes involved in the life cycle of
188 cumulus clouds. This model considers two concentric cylinders. The inner cylinder has a radius 10 times smaller than the outer cylinder. In the inner cylinder,
189 the vertical velocity of the flows is determined by solving a simplified form of the Navier-Stokes equations, coupled with the energy conservation equation.
190 The outer cylinder serves primarily for guaranteeing the condition of zero velocity divergence (continuity equation for incompressible flow). To this end, a
191 radial velocity component is introduced at the interface between these two cylinders (hence the expression of a 1.5D model), diagnosed from the
192 convergence or divergence layers and allowing entrainment from the environment. In this environment the only variable updated in this outer cylinder is
193 the vertical velocity in order to evaluate the radial gradient in vertical velocity and the subsequent turbulent flux; all the other variables are assumed to be
194 unaffected by the cloud processes within the inner cylinder and kept constant throughout the simulation.

195 All the microphysical processes detailed in the previous section and summarised in Figure 2 are calculated only in the central cylinder. Thus, this is also in
196 the inner cylinder, for each grid layer, that phase changes in the water will be computed with the subsequent absorption or release of latent heat that will
197 alter the buoyancy of the air and which ultimately generate the updraft and downdraft motions.

198 2. Applications

199 To establish a theoretical scavenging coefficient scheme, the entire previously detailed methodology is applied to two very different idealised case studies
200 representative of two different types of clouds. First, we will model a vigorous cumulonimbus, then a shallow stratus. These two cloud types were selected
201 as they present, respectively, the higher and lower values, in terms of vertical extension, relative humidity, and rainfall intensity. Furthermore, while the
202 stratus that we simulate is shallow enough to be a warm cloud, cold microphysical processes are essential to capture the development of the cumulonimbus
203 situation.

204

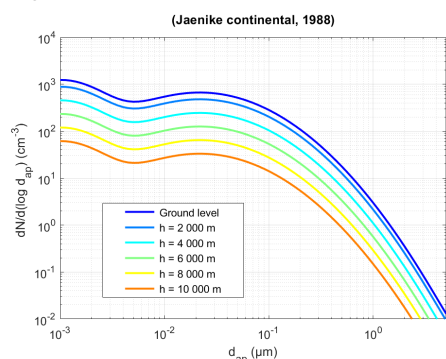


205

2.1. Application to a cumulonimbus

206 Description of the cumulonimbus considered

207 The cloud selected to model the cumulonimbus is the episode of 19 July 1981 of the CCOPE campaign (Cooperative Convective Precipitation Experiment;
208 Knight 1982 and Dye *et al.*, 1986), which took place near Miles City in Montana (USA). This episode was selected because it is very finely documented and
209 this episode is a test case for many codes simulating the formation of convective clouds, and in particular the DESCAM model (Flossmann & Wobrock, 2010).
210 A Radio sounding taken at Miles City at 16h00 local time (just before the storm) is used to initialise the thermodynamic conditions of the atmospheric
211 column: temperature and humidity. For the vertical pressure profiles, standard conditions are assumed. In addition, we used the observations of both two
212 Doppler radars measured high-resolution reflectivity as well as the movements of the cloud and five aircrafts that were able to make numerous passes
213 through the cloud throughout its maturation and through to the precipitation episodes. The spatial-temporal evolution of the thermodynamic conditions,
214 associated with the microphysical properties of the cloud system, and the atmospheric flows are therefore recorded in fine detail for the entire life of this
215 cumulonimbus and can be used to evaluate the model performance to capture the clouds physics. For this article, we therefore used the same modelling
216 hypotheses as those detailed by Leroy *et al.*, (2006). Convection was triggered by +2.3°C heating of the ground during the first 10 minutes of the simulation.
217 During this campaign, no physical-chemical measurements were made of the aerosols, hence we consider that they consisted of ammonium sulphate ($\kappa =$
218 0.61 and $\rho_{\text{dry}} = 1.77 \cdot 10^3 \text{ kg.m}^{-3}$ Petters and Kreidenweis, 2007) with an initial particle size distribution of the Jaenicke continental type (1988). We considered
219 a homogeneous distribution in the atmospheric boundary layer (i.e., over the first 3 kilometres), then above the concentration is assumed to decrease
220 exponentially with a scale height of 3000 m (Figure 4).



221

222

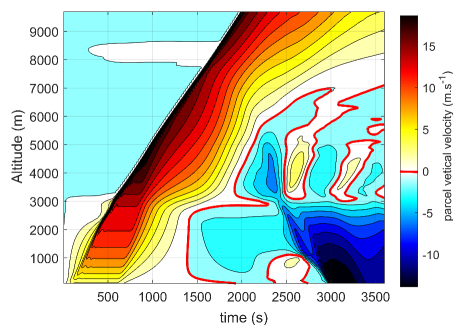
Figure 4. Initial particle size distribution of aerosols considered for this simulation

223

The simulation lasted 3600 s, on a 10 km high column. The spatial and temporal resolutions were set to 100 m and three seconds respectively.

224

Figure 5 and Figure 6 show respectively the spatial-temporal evolutions of the vertical flows in the central cylinder and the liquid water and ice content.



225

226

Figure 5. Spatial-temporal distribution of the vertical components of atmospheric flows. The thick line in red separates the updraft ($w_{\text{air}} > 0$) flows from the downdraft flows ($w_{\text{air}} < 0$).

227

228

229

In these figures, we can see that the initial superheating of the air layer at ground level induces an updraft flow due to buoyancy forces. Approximately 500 s after the start of the simulation, the air reaches critical supersaturation at an altitude of 3000 m and the aerosols are gradually converted into droplets. The spatial-temporal distribution shown on the left of Figure 6 highlights the appearance of a cloud at the spatial-temporal coordinate (500 s, 3000 m). Vapour condensation induces a latent heat release, which in turn increases buoyancy of the air parcel, accelerating the updraft flows (approx. 15 m.s^{-1} at 4000 m).

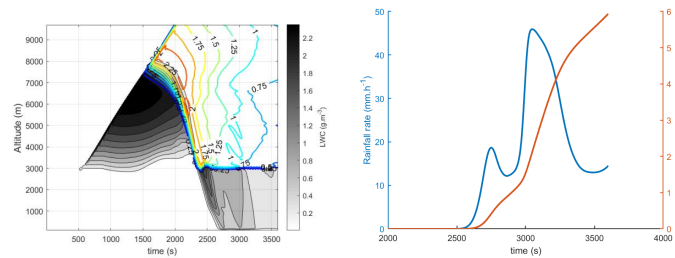
230

231

232



233 This flow transports the vapour at altitude and by cooling this induces the progressive activation of the aerosols, and a vertical extension of the cloud. Near
 234 7000 m, the first ice crystals are formed. The coexistence of ice crystals and supercooled droplets will allow rapid crystal growth at the expense of the
 235 droplets (best known as the WBF mechanism for: Wegener, 1911; Bergeron, 1928; Findeisen, 1938 processes). Then, the crystals begin to precipitate at
 236 around 1700 s since they reach sizes large enough for gravity to undertake updraft speed. In precipitating, the larger crystals collect the suspended droplets.
 237 Hence, under the coupled influence of the Wegener - Bergeron - Findeisen effect and, above all, the collection of droplets by the ice particles, after 2200
 238 seconds of simulation the cloud only contains ice. Finally, below an altitude of 3000 m, the solid hydrometeors melt and liquid precipitation forms. Figure 6
 239 shows on the right the rainfall intensities, as well as the cumulative precipitation calculated by the model at ground level. This timeline presents two local
 240 maxima: the first at 2750 s after the start of the simulation, corresponding to an intensity of 18 mm.h⁻¹ and the second 300 s later, with an intensity of about
 241 46 mm.h⁻¹.



242

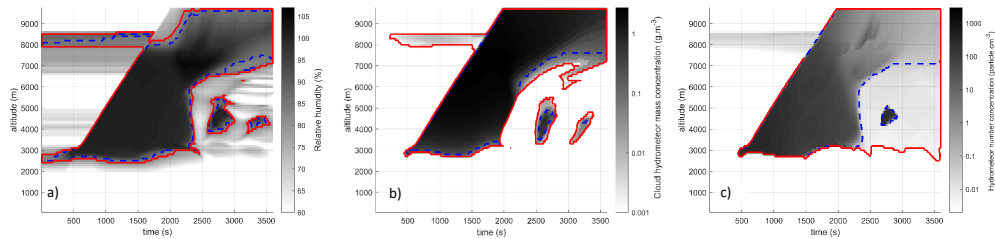
243 Figure 6. On the left: Spatial-temporal distributions of liquid water content (LWC, greyscale) and ice content (IWC, iso-contours).
 244 On the right: Temporal evolution of rainfall intensity and cumulative precipitation at ground level

245 **Calculation of the scavenging coefficient**

246 Based on this modelling results, we applied all the methodology described in section 1.1. The first step consisted in establishing the contours of the cloud,
 247 in order then, using Equation 3 integrated over the entire aerosol distribution, to be able to calculate the equivalent cloud scavenging coefficient.

$$\Lambda_{cloud}(d_{ap}) = - \frac{1}{dt} \frac{dM}{\langle M \rangle}_{cloud} = \frac{\phi_{ap, precip}}{\langle M \rangle \cdot H_{cloud}} \quad \text{Equation 15}$$

248 As already indicated in section 1.2, there is no strict definition of the boundaries of the cloud, particularly at the interface with the precipitation, and it can
 249 also be observed in Figure 6 that the total water content does not show any demarcation between the cloud and the precipitation. Moreover, as Spänkuch
 250 *et al.*, (2022) point out, the physical phenomenon studied will determine which contours are the most relevant. Therefore, for this study, we examined three
 251 of the physical parameters to establish this contour. These three criteria are the relative humidity of the air parcel (calculated in relation to liquid water),
 252 the mass concentration of hydrometeors with a diameter of less than 64 µm and, lastly, the concentration of hydrometeors. The contours of this
 253 cumulonimbus are presented in Figure 7 for each of these criteria, each with two thresholds considered.



254

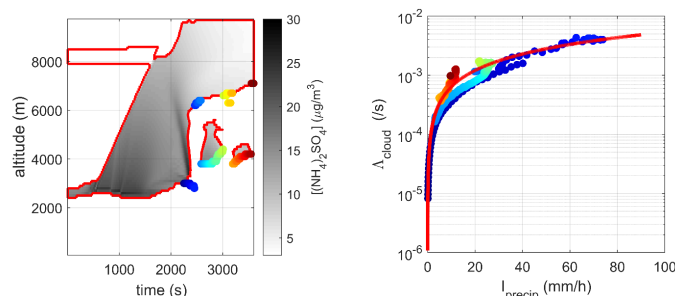
255 Figure 7. Test of different criteria to establish the contours of the simulated cumulonimbus.

- 256 a) threshold based on relative humidity: (---): $RH > 85\%$; (—): $RH > 80\%$.
 257 b) threshold based on the total water content of hydrometeors with a diameter less than 64 µm: (---): Mass concentration of cloud
 258 hydrometeors $> 0.1 \text{ g} \cdot \text{m}^{-3}$;
 259 (—): Mass concentration of cloud hydrometeors $> 0.001 \text{ g} \cdot \text{m}^{-3}$
 260 c) threshold based on number concentration of total hydrometeors: (---) $\int dN + dR > 0.03 \text{ cm}^{-3}$
 261 (—): $\int dN + dR > 0.003 \text{ cm}^{-3}$

262 We can see in this figure that, apart from the criterion based on the concentration of hydrometeors (Equation 9), with a threshold of 0.003 hydrometeors
 263 per cubic centimetre, all the other criteria yield very similar contours. Thus, the cloud forms close to an altitude of 3000 m and its base remains constant for
 264 up to 2500 s of simulation. During these 2500 s, the cloud thickens vertically until it reaches the tropopause (considered to be at 10,000 m in this calculation).
 265 As shown in Figure 6 (on the right), 2500 s corresponds to the start of precipitation. This moment corresponds to an elevation of the base of the cloud up to
 266 about 7000 m, except for the last criterion ($N_{hydrometeor} > 0.003 \text{ cm}^{-3}$), for which the height of the base of the cloud remains constant close to the
 267 altitude of 3000 m, even during rain.

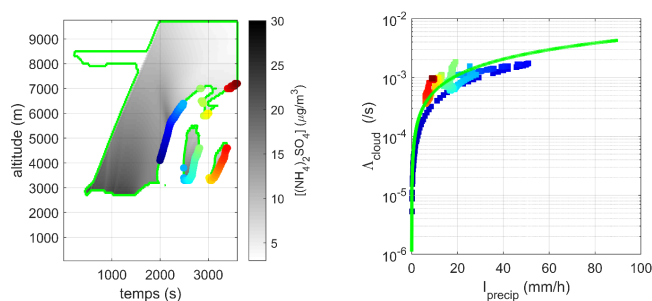


268 Initially, our objective was to find a bijective relationship between a set of meteorological parameters available in DESCAM and the scavenging coefficient
 269 calculated by this methodology. Most often in the literature, cloud scavenging is described as a power function of precipitation intensity (Hertel *et al.*, 1995;
 270 MRI, 2015; Leadbetter *et al.*, 2015; Groell *et al.*, 2014; Querel *et al.*, 2021). Figure 8, Figure 9 and Figure 10 respectively present the contours of the cloud
 271 established on the basis of the three criteria previously introduced (Figure 7). Within these contours, we calculated the total mass concentration of
 272 ammonium sulphate ($\mathcal{M}(z)$), adding together the respective concentrations of the aerosol phases ($\mathcal{M}_{int}(z)$), in the droplets ($\mathcal{M}(z)$) and in the crystals
 273 ($\mathcal{M}(z)$). Knowing the flux of ammonium sulphate that is within the precipitative hydrometeors through the base of the cloud (Equation 6, Equation 7 and
 274 Equation 8), we could deduce the scavenging coefficient, which we plotted according to the precipitation intensity calculated at the base of the cloud. Like
 275 Costa *et al.*, (2010), Stephan *et al.*, (2008) and Qu  rel *et al.* (2021), a threshold of $0.1 \text{ mm} \cdot \text{h}^{-1}$ was considered in order to limit noise. In Figure 8, 9, 10, the
 276 correspondence of the dots can be deduced with the colour codes of the points. On the left-hand side, the identification of the spatial-temporal coordinates
 277 where precipitation and scavenging coefficient are calculated is plotted. On the right-hand side, the corresponding relationship between scavenging
 278 coefficient and precipitation intensity can be read. These results are of great importance because they show that the relationship between the scavenging
 279 coefficient and the rainfall intensity is the same at the beginning and the end of the rainfall episode. In addition, an adjustment by a power law is determined
 280 for each contour. The coefficients for these adjustments are shown in Table 1.



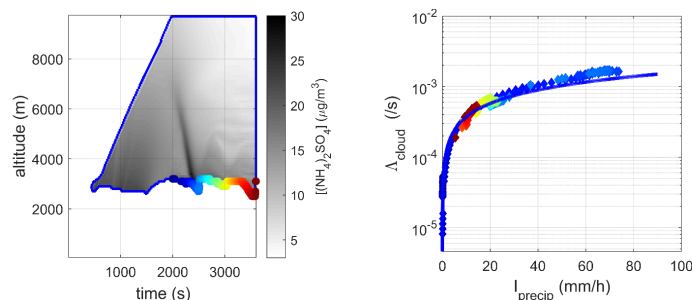
281

282 Figure 8. On the left: spatial-temporal distribution of the ammonium sulphate concentration in the cloud contour (— cloud contour for a
 283 relative humidity greater than 80%). On the right: correlation between the scavenging coefficient and the precipitation intensity determined
 284 at the base of the cloud, (—) adjusted by a power law



285

286 Figure 9. On the left: spatial-temporal distribution of the ammonium sulphate concentration in the cloud contour (— cloud contour for a
 287 mass concentration of cloud hydrometeors greater than $0.001 \text{ g} \cdot \text{m}^{-3}$). On the right: correlation between the scavenging coefficient and the
 288 precipitation intensity determined at the base of the cloud, (—) adjusted by a power law



289

290 Figure 10. On the left: spatial-temporal distribution of the ammonium sulphate concentration in the cloud contour (— cloud contour for a
 291 concentration in number of hydrometeors greater than $0.003 \text{ particles} \cdot \text{cm}^{-3}$). On the right: correlation between the scavenging coefficient
 292 and the precipitation intensity determined at the base of the cloud, (—) adjusted by a power law



293

294 In these three figures, we observe that the relationship linking the intensity of precipitation to the scavenging coefficient by the cloud is fairly insensitive to
295 the definition selected to describe its contour. Moreover, the power law adjustments plotted in Figure 8, Figure 9 and Figure 10 are very similar (Table
296 **1** **Erreur ! Source du renvoi introuvable.**). Nevertheless, only the last contour, based on the hydrometeors concentration (and with a threshold of
297 0.003 m^{-3}), gives a perfectly bijective relationship between the precipitation intensity at the base of the defined contour and the scavenging coefficient.
298 This result is surprising because, as previously mentioned in section 1.3, the driving mechanism for in-cloud scavenging is at first order the activation (which
299 is driven by the supersaturation level and physical-chemical properties of the aerosols, Flossmann and Wobrock, 2010). It would therefore seem logical that
300 a criterion based on the relative humidity in the grid cell would be the most relevant. However, it is the criterion based on the concentration of hydrometeors
301 that is the more reliable. This is because there are zones in the cloud where the humidity is too low to activate the aerosols (e.g., at 4000 m at 2500 s where
302 $\text{RH} < 85\%$, or indeed Figure 7a), but where there is a significant number of droplets and crystals ($> 0.03 \text{ cm}^{-3}$). These droplets and crystals have been activated
303 elsewhere and previously, but they nevertheless continue to collect aerosols around them – for example by Brownian capture, contributing to scavenging.
304 It therefore seems justified to define a cloud contour based on a diagnostic of the numeric concentration of hydrometeors.

305

306

Table 1: Power law adjustment associated with each of the cloud contours studied

Contour type	Power law adjustments
Based on relative humidity (Figure 8)	$\Lambda_{cloud} = 7.6 \times 10^{-5} I^{0.92}$
Based on mass concentration of cloud hydrometeors (Figure 9)	$\Lambda_{cloud} = 7.2 \times 10^{-5} I^{0.9}$
Based on numeric concentration of hydrometeors (Figure 10)	$\Lambda_{cloud} = 8.6 \times 10^{-5} I^{0.6}$

307

308 However, this numeric concentration criterion, although more precise for theoretically assessing the scavenging coefficient, is not easily accessible in a crisis
309 code. Nevertheless, detailed analysis of the results of these simulations seems to show that it would be wise to define the cloud base as being constant and
310 equal to the altitude at which critical supersaturation was first reached, i.e., the altitude at which the cloud began its formation.

311

312 2.2. Application to a stratus

313 Description of the stratus considered

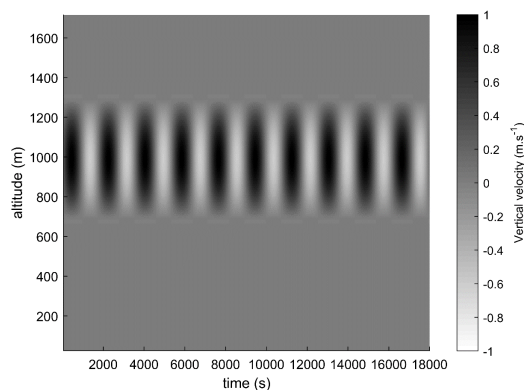
314 The same approach as above was considered for modelling scavenging by a shallow stratus cloud. The main differences with the previous modelling (i.e., of
315 the cumulonimbus) beyond the initialisation of thermodynamical profile is the treatment of the vertical advection within the cloud. Whereas, for the
316 previous modelling, differences in air buoyancy (related to the initial thermal gradients and latent heat released by water phase changes) were the cause of
317 vertical velocities and could be described and captured by the dynamics of the model, when it comes to modelling this stratus, the dynamics is forced by
318 large scale features that are not included in the 1,5D model. Therefore, the idea is to prescribe totally the time evolving profile for vertical velocity to model
319 this forcing. Since the convection is more forced that triggered by buoyancy, prescribing it and not computing the microphysical feedback on dynamics is
320 reasonable. For the scenario, we considered the vertical advection model proposed by Zhang *et al.*, (2004) and recapitulated in Equation 16. We therefore
321 imposed a sinusoidal profile vertical velocity, with the maximum that oscillates from positive to negative values with a time period of 1800 s. The maximum
322 of the velocities was located at the altitude (z_c) of 1000 m and vertical motions allowed between 700 and 1300 m ($h_c = 600$ m, Figure 11). Like Zhang *et al.*,
323 (2014), in the advection model, we imposed an average updraft velocity (w_0) of 0.2 m.s^{-1} and an oscillation amplitude (w_1) of 0.8 m.s^{-1} at an altitude of
324 1000 m. Figure 5 shows the spatial-temporal distribution of vertical flows prescribed in the central cylinder. The temperature profile follows a dry adiabatic
325 lapse rate with a temperature of 15°C on the ground so that there are no negative temperatures in the cloud. Above 1300 m, like Zhang *et al.* (2014), we
326 imposed an inversion of the thermal profile. At altitudes between 700 and 1300 m, the relative humidity was initialised at 98.5%, and 95% outside of this
327 range. For the aerosols, the initial conditions were identical to those for cumulonimbus (Equation 5).



$$\begin{cases}
 w(z, t) = \cos\left(\pi \frac{z - z_c}{h_c}\right) \left[w_0 + w_1 \sin\left(\frac{2\pi t}{t_c}\right) \right] & \text{if } |z - z_c| \leq \frac{h_c}{2} \\
 w(z, t) = 0 & \text{if } |z - z_c| > \frac{h_c}{2}
 \end{cases}$$

Equation 16

$z_c = 1000 \text{ m}; h_c = 600 \text{ m}; t_c = 1800 \text{ s}; w_0 = 0.2 \text{ m} \cdot \text{s}^{-1}; w_1 = 0.8 \text{ m} \cdot \text{s}^{-1}$



328

329

Figure 11. Spatial-temporal distribution of the vertical components of atmospheric flows (Zhang *et al.*, 2004)

330

331

332

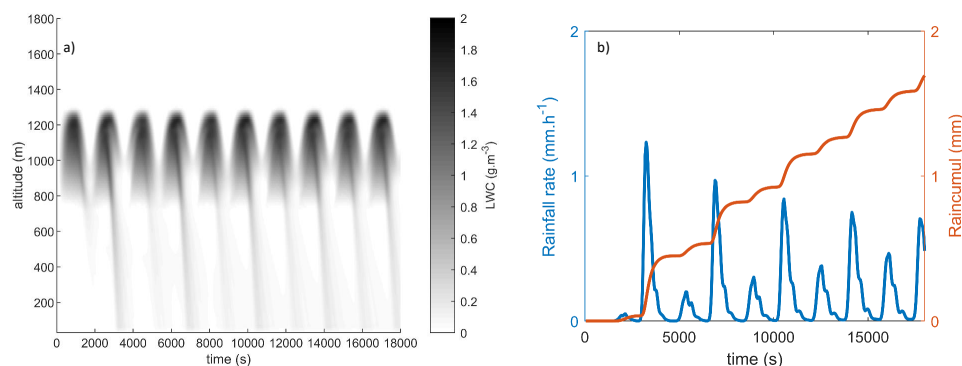
333

334

335

336

Figure 12 shows on the left the spatial-temporal distribution of the water content calculated by DESCAM. The critical supersaturation was reached close to the altitude of 700 m from the first updraft phase (0–1000 s). The LWC then increased with altitude throughout the phase where the atmospheric flows were ascending. At the cloud summit, the liquid water content reached approximately $1.6 \text{ g} \cdot \text{m}^{-3}$. Conversely, during the downdraft phases, the supply of dry air to lower altitudes induced, due to the temperature profile considered, a drop in the relative humidity, which in turn induced evaporation of the droplets, resulting in a significant reduction in the LWC. These downdraft phases also had the effect of advecting droplets below the cloud band. During the period of velocity oscillations ($t < t_c$), this precipitation completely evaporated before reaching the ground. However, from the second period onwards, rain was diagnosed on the ground (Figure 6. b).



337

338

339

Figure 12. On the left: Spatial-temporal distribution of the liquid water content calculated by DESCAM (LWC, in greyscale).
 On the right: Temporal evolution of rainfall intensity and cumulative precipitation diagnosed by DESCAM at ground level

340

341

The DESCAM model predicts intermittent precipitation at ground level with flurries of precipitation in the order of a millimetre per hour. Over a precipitation period of approximately four hours, the cumulative precipitation was only approximately 3 mm.

342

343

344 Calculation of the stratus scavenging coefficient

345

346

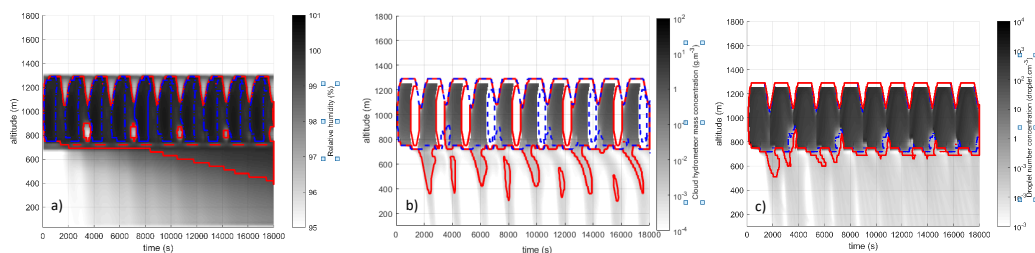
347

348

As before in the case of cumulonimbus, it is necessary to define the contours of the cloud. We therefore used the three criteria previously introduced and look for the one with the clearest demarcation line between the cloud zone and the precipitation zone, in order to apply a dedicated scavenging coefficient (Figure 13). As before, we observe from Figure 12.a that water content is not a good indicator to outline the cloud boundaries. Indeed, no discontinuity is observed for this parameter enabling demarcation between the cloud and the precipitation.



349



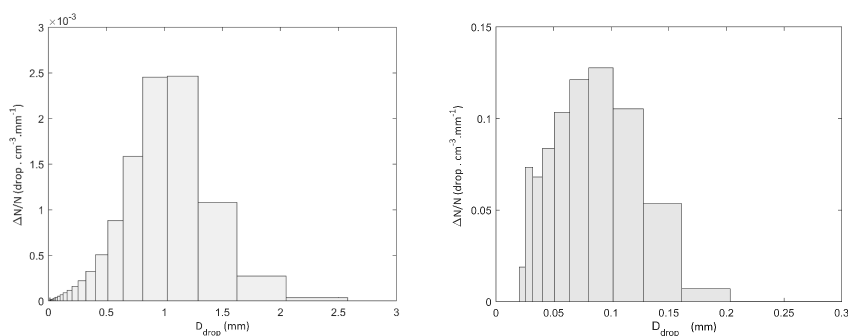
350

351 **Figure 13. Test of different criteria to establish the contours of the simulated stratus.**
 352 a) threshold based on relative humidity: (---): $RH > 99\%$ (—): $RH > 100\%$.
 353 b) threshold based on the mass concentration of hydrometeors with a diameter less than $64 \mu m$: (---): Mass concentration of cloud
 354 hydrometeors $> 0.01 g \cdot m^{-3}$;
 355 (—): Mass concentration of cloud hydrometeors $> 0.001 g \cdot m^{-3}$
 356 c) threshold based on the concentration of hydrometeors: (---): $\int dN > 0.1 cm^{-3}$
 357 (—): $\int dN + dR > 0.03 cm^{-3}$

358

359 Based on these results, it is more difficult to delineate the contours of this stratus than for the cumulonimbus. This is because, for these three criteria, only
 360 the droplets concentration shows a clear demarcation between precipitation and cloud zone. Moreover, only this criterion gives stable cloud contours,
 361 regardless of the threshold value selected. This difference with respect to the cumulonimbus is mainly due to the size of the precipitating hydrometeors,
 362 which are much larger in the case of cumulonimbus. Figure 14 shows that the particle size distribution mode in number of raindrops, for the cumulonimbus,
 363 is close to a diameter of 1 mm, whereas it is $100 \mu m$ for the stratus. It is therefore easier with a cumulonimbus than with a stratus to define a size threshold
 364 distinguishing droplet (belonging to the cloud) from raindrops (belonging to precipitation). The criterion based on the mass concentration of hydrometeors
 365 exceeding $64 \mu m$ is therefore less effective under a stratus than under a cumulonimbus. To explain the poor performance of the criterion based on relative
 366 humidity, again it is the particle size that counts. As the droplets under the stratus are smaller than under the cumulonimbus, their drop velocities are lower,
 367 and they reside longer in the atmosphere – about 10 times longer. This longer residence time promotes the increase in relative humidity under the cloud,
 368 and humidity saturation under the cloud. This makes it difficult to use this criterion to determine the boundary between rain and cloud for a stratus.

369

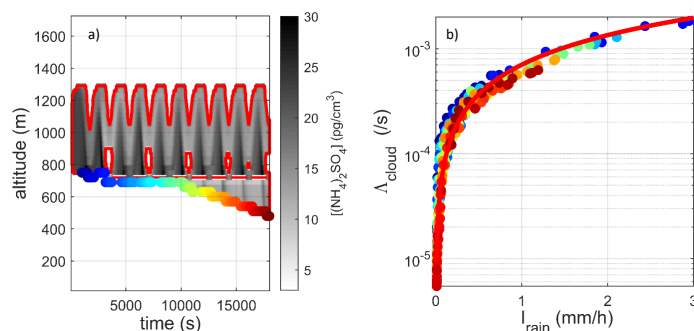


370

371 **Figure 14. Particle size distributions of raindrops determined by the DESCAM model at ground level**
 372 Left: For cumulonimbus at time $t=3000$ s
 373 Right: For cumulonimbus at time $t=8200$ s

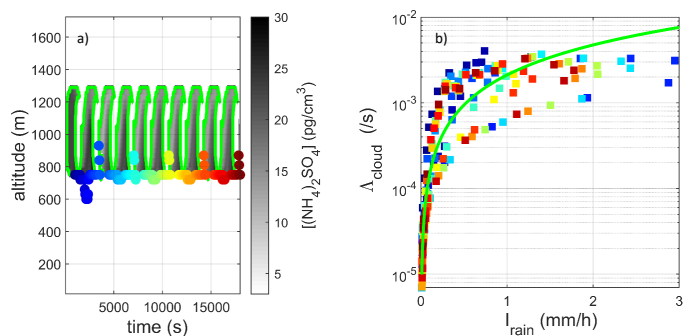
374

375 As previously, for the cumulonimbus, we search for a criterion to delimit cloud from rain. Same parameters as in section 2.1 are investigated and
 376 presented in Figure 15, 16 and 17.



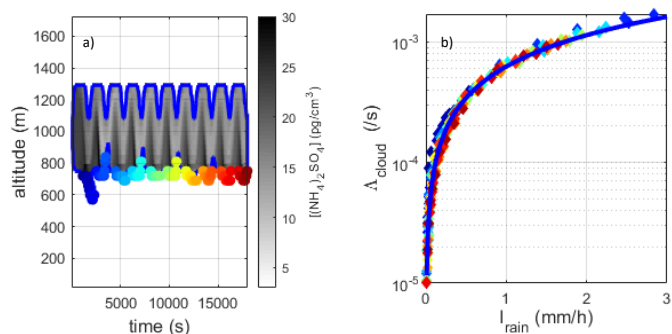
377

378 Figure 15. On the left: spatial-temporal distribution of the ammonium sulphate concentration in the cloud contour (— cloud contour for a
 379 relative humidity above 99%). On the right: correlation between the scavenging coefficient and the precipitation intensity determined at the
 380 base of the cloud, (—) adjusted by a power law



381

382 Figure 16. On the left: spatial-temporal distribution of the ammonium sulphate concentration in the cloud contour (—) criterion based on the
 383 mass concentration of hydrometeors with a diameter greater than $64 \mu\text{m}$ with a threshold set at $0.01 \text{ g}\cdot\text{m}^{-3}$. On the right: correlation
 384 between the scavenging coefficient and the precipitation intensity determined at the base of the cloud, (—) adjusted by a power law



385

386 Figure 17. On the left: spatial-temporal distribution of the ammonium sulphate concentration in the contour of the cloud (criterion based on
 387 the concentration of hydrometeors with a threshold set at $0.01 \text{ particle}\cdot\text{cm}^{-3}$). On the right: correlation between the scavenging coefficient
 388 and the precipitation intensity determined at the base of the cloud, (—) adjusted by a power law

389

390 In these three figures, we observe that the contour introduced by Hiron (2017) for cumulonimbus (based on a separation between cloud water and
 391 precipitation water, on the basis of a criterion on the size of hydrometeors, cf. section 1.2) is no longer applicable for the stratus, and gives highly dispersed
 392 scavenging coefficient results, particularly for low rain intensity ($I < 2 \text{ mm}\cdot\text{h}^{-1}$). This is because, for this status, it is difficult to establish a strict boundary



393 between a raindrop and a cloud droplet, based on their size. However, the other two criteria yield bijective and similar relationships, both in terms of
 394 cloud contours (Figure 15.a and Figure 17.a) and the adjusted power laws (Table 2). Unlike cumulonimbus, stratus contours appear to be reliable using a
 395 criterion based on relative humidity. This difference is related to the intensities of vertical flows in the cumulonimbus. Indeed, we observe in Figure 5 that,
 396 in the simulated cumulonimbus, the downdraft flows can be very intense (up to $5 \text{ m}\cdot\text{s}^{-1}$), transporting to the base of the cloud air masses with a lower mixing
 397 ratio and hence lower relative humidity.

398 Table 2. Adjustment of scavenging coefficients by power laws for the three types of contours studied

Contour type	Power law adjustments
Based on relative humidity (Figure 15)	$\Lambda_{cloud} = 7.03 \times 10^{-4} J^{0.94}$
Based on mass concentration of cloud hydrometeors (Figure 16)	$\Lambda_{cloud} = 2.10 \times 10^{-3} J^{1.16}$
Based on hydrometeor concentration (Figure 17)	$\Lambda_{cloud} = 6.24 \times 10^{-4} J^{0.86}$

399

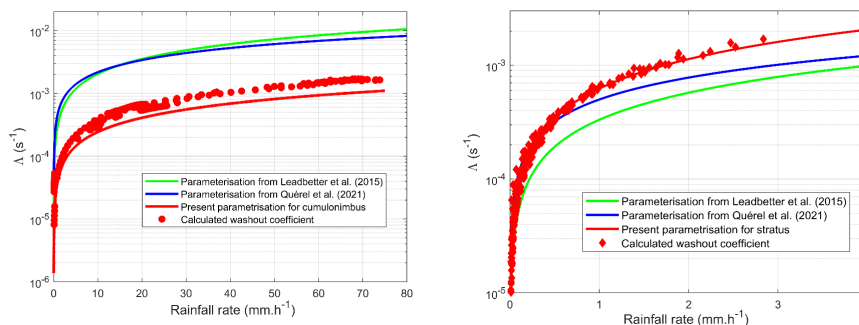
400

401 These calculations show that, regardless of the type of simulated cloud, cumulonimbus or stratus, the criterion based on the hydrometeor concentration
 402 makes it possible to yield cloud contours that are both stable (with little variation when the threshold value is varied), and for which the relationship between
 403 the scavenging coefficient and the rainfall intensity is the most biunivocal (Figure 8, Figure 9 and Figure 10 for cumulonimbus and Figure 15, Figure 16 and
 404 Figure 17 for stratus). This criterion is not directly accessible in meteorological models; however, examination of Figure 10 and Figure 17 suggests that the
 405 cloud base remains stable over time. It would therefore be possible to assess the altitude at which critical supersaturation is reached, and to consider this
 406 altitude constant over a period that depends on the ratio between the size of the grid cell and the velocity of the horizontal flows.

407

408 2.1. Comparison with the literature

409 In order to comfort our theoretical findings with observations, we lack data. There is very little number of experiments to establish *in situ* scavenging
 410 coefficients for different types of clouds. Based on caesium-137 deposition measured following the Fukushima Daiichi accident, Leadbetter *et al.*, (2015)
 411 used the Met Office dispersion model: NAME (Numerical Atmospheric-dispersion Modelling Environment) for the dispersion of the radioactive plume
 412 emitted during the accident, considering the meteorological data from the ECMWF model. The authors managed to determine the cloud scavenging
 413 coefficient which best suits the ground measurements of deposition (Kinoshita *et al.*, 2011). In the same general approach, but using the IRSN LdX dispersion
 414 model (Quélo *et al.*, 2007 and Groëll *et al.*, 2014) and meteorological data from MRI (Sekiyama *et al.*, 2017), Quérel *et al.* (2017) established a very similar
 415 scavenging coefficient. These two schemes are compared in Figure 18.



416

417 Figure 18. Comparison of the parameterisations established respectively for a cumulonimbus (left) and a stratus (right) with the
 418 parameterisations established by Leadbetter *et al.*, 2015 and Quérel *et al.*, 2021 following the Fukushima accident

419



420 In this figure, we observe that the application of our scheme to a stratus (Figure 18, on the right), concurs excellently with the parametrisation of scavenging
421 by clouds established following the Fukushima accident; in particular the parametrisation of Querel *et al.*, 2021. Nevertheless, the application of our
422 approach to cumulonimbus presents much greater differences. Indeed, over the entire rainfall intensity range, our results are on average six times lower
423 than the correlations of Leadbetter *et al.*, (2015) and Querel *et al.*, (2015). Two questions therefore arise:

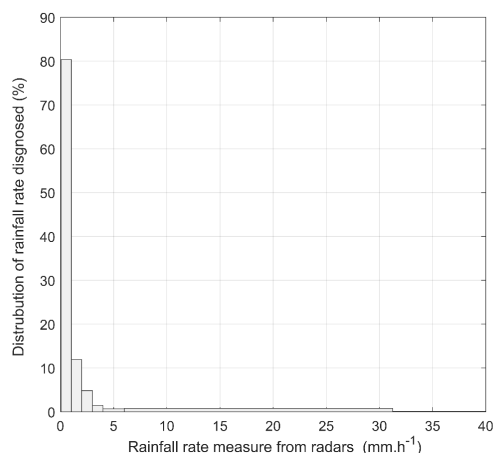
424 First of all, was there scavenging by cumulonimbus during the Fukushima accident? This would explain why it is difficult to compare our parametrisation of
425 scavenging by cumulonimbus with those deduced during the Fukushima accident.

426 Next, why, for the same rainfall intensity, do our calculations show that cumulonimbus scavenges less than stratus?

427 We will therefore address these two questions.

428 **Was there scavenging by cumulonimbus during the Fukushima accident?**

429 To answer this question, let us consider the distribution of rainfall intensities diagnosed from radar measurements by Saito *et al.*, (2015) during March 2011
430 in the Fukushima region (Figure 19). These results show that 80% of rain episodes diagnosed corresponded to rainfall intensities of less than 1.5 mm.h^{-1} ,
431 and 97% to intensities of less than 3.5 mm.h^{-1} (range of rainfall intensity produced at the base of the simulated stratus, Figure 15) and less than 0.01% had
432 intensities of more than 10 mm.h^{-1} . In view of these results, it is not possible to completely exclude the presence of rain issuing from cumulonimbus over
433 the period of the accident; however, if there was any, its contribution to the construction of the parameterisation of Leadbetter *et al.* (2015) and Querel *et*
434 *al.* (2021) is negligible.



435

436 Figure 19. Distribution of rainfall intensity measured in the Fukushima region during March 2011 (Sekiyama *et al.*, 2017)

437

438 **Why, for the same rainfall intensity, do our calculations show that cumulonimbus scavenges less than stratus?**

439 This result is not intuitive. The level of supersaturation of cumulonimbus (Figure 7.a) is much higher than that of stratus (Figure 13.a), therefore the critical
440 activation diameter for cumulonimbus is smaller than that of stratus (Figure 3); it would therefore be expected, contrary to what is observed in Figure 18,
441 that the scavenging coefficient by cumulonimbus would be slightly greater than that of stratus. It seems that this result is linked to the fact that we are
442 seeking to parameterise the scavenging coefficient by the intensity of precipitation. Hence, if the supersaturation is higher, as is the case for cumulonimbus,
443 for the same activated aerosol mass, these particles are diluted in a larger mass of water, as the condensation is also much greater (in reality, the activated
444 aerosol mass increases significantly since, as we have indicated previously, the activation diameter of the aerosols decreases as supersaturation increases).
445 Let us therefore examine the impact of this effect of vapour condensation on the deduced parameterisation. In the DESCAM model, condensation is
446 modelled by Equation 17. This equation is taken from Pruppacher *et al.* (1998, chapter 13, section 2). It results from the vapour diffusion equation on a
447 droplet of diameter D_{drop} in the air with supersaturation S and temperature T_{∞} , considering the thermodynamic equilibrium of the suspended drop within
448 air using the κ -Köhler theory.



$$\left\{ \begin{aligned} \frac{dD_{drop}}{dt} &= \frac{4}{D_{drop}} \frac{\rho_w \mathcal{R} T_\infty}{p_{sat,w} \mathcal{D}_v M_w} + \frac{O_n \rho_w}{k T_\infty} \left(\frac{O_n \rho_w}{\mathcal{R} T_\infty} - 1 \right) \\ y &= \frac{4 \sigma_w \mathcal{D}_{drop} M_w}{\rho_w \mathcal{R} T_\infty D_{drop}} - K \frac{d_{ap}^{dry^3}}{D_{drop}^3} \end{aligned} \right. \quad \text{Equation 17}$$

449

450 In this equation \mathcal{R} is the perfect gas constant, $p_{sat,w}$ the saturating vapour pressure, d_{ap}^{dry} the dry diameter of the aerosol, O_n the latent heat of
 451 vaporisation of the water, $\sigma_w \mathcal{D}_{drop}$ the surface tension, k the thermal conductivity of the air, M_w and ρ_w the molar mass and density of the water vapour,
 452 and finally \mathcal{D}_v the diffusion coefficient of the vapour in water in the air. As the Kelvin effect (linked to the curvature of the interface) and the solute effect
 453 become very quickly negligible after activation of the aerosol, this equation can be greatly simplified and reduced to: $D_{drop} dD_{drop} = \mathcal{C} \cdot s_{v,w} dt$, where \mathcal{C} is a
 454 constant, enabling it to be integrated analytically, to give: $D_{drop}(t) = \sqrt{D_{drop,t_0}^2 + 2\mathcal{C} \cdot s_{v,w} \cdot t}$. Thus, to assess the effect of dilution of the aerosol in the
 455 droplet due to condensation, we can write:

$$\frac{D_{drop}(t)_{stratus}^2}{D_{drop}(t)_{cumulonimbus}^2} = \frac{D_{drop,t_0}^2 + 2\mathcal{C} \cdot \langle S \rangle_{stratus} \cdot t_{stratus}}{D_{drop,t_0}^2 + 2\mathcal{C} \cdot \langle S \rangle_{cumulonimbus} \cdot t_{cumulonimbus}} \quad \text{Equation 18}$$

456

457 Attention: In this equation, $D_{drop}(t)_{stratus}$ and $D_{drop}(t)_{cumulonimbus}$ are not the diameters of the droplets in the stratus and in the cumulonimbus, but
 458 the diameters they would have had, if only the condensation mechanism had caused them to grow. We are in fact seeking to assess how large will be the
 459 dilution of aerosol material in the droplets related to vapour condensation. There are other mechanisms modelled in DECAM (such as coalescence or riming,
 460 Figure 2) that lead to the growth of hydrometeors, without necessarily diluting the aerosols in the droplets. If there had only been the condensation
 461 mechanism, we could have used Figure 14 directly to assess this dilution.

462 For long periods of time, further simplification can still be made because $D_{drop,t_0}^2 \ll D_{drop}(t)_{stratus}^2 < D_{drop}(t)_{cumulonimbus}^2$. Finally, we can write:

$$\frac{D_{drop}(t)_{stratus}^2}{D_{drop}(t)_{cumulonimbus}^2} = \frac{\langle S \rangle_{stratus} \cdot t_{stratus}}{\langle S \rangle_{cumulonimbus} \cdot t_{cumulonimbus}} \quad \text{Equation 19}$$

463 In this equation, the times $t_{stratus}$ and $t_{cumulonimbus}$ are therefore the times necessary for the formation of precipitation under the cloud. For each of the
 464 types of cloud, we observe in Figure 6.a and Figure 12.a that these times are very similar (≈ 2200 s), which allows us to write:

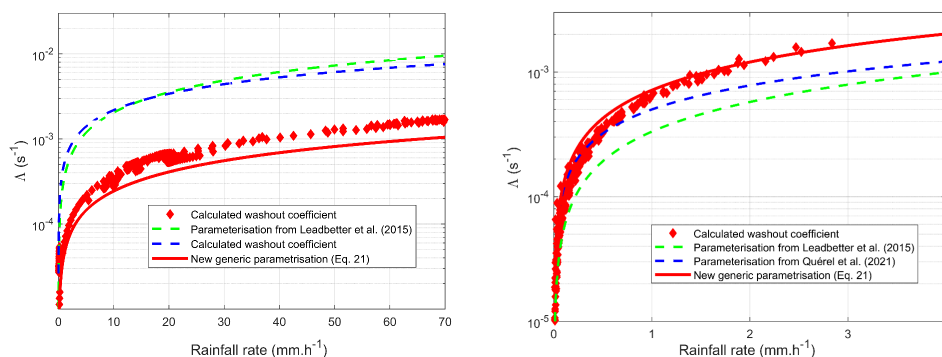
$$\frac{D_{drop}(t)_{stratus}}{D_{drop}(t)_{cumulonimbus}} = \sqrt{\frac{\langle S \rangle_{stratus}}{\langle S \rangle_{cumulonimbus}}} \quad \text{Equation 20}$$

465 The numerical application of this equation highlights a condensation growth ratio of a factor 2.3 between cumulonimbus and stratus. In mass, this coefficient
 466 corresponds to a dilution factor of 12. However, Figure 18 shows that, with this new approach, we can calculate that cumulonimbus scavenges 6 times less
 467 than stratus. This explanation is therefore satisfactory in view of all the hypotheses that have been made, especially since we have considered that the
 468 activated aerosol mass remained constant when supersaturation increased. We therefore propose a new generic parametrisation to any type of cloud,
 469 which this time takes into account this condensation-related dilution effect, Equation 21. This scavenging scheme is therefore corrected by a coefficient
 470 $1/\langle S \rangle_{cloud}^{3/2}$ which characterises the dilution related to the growth of droplets by condensation:

$$\Lambda_{cloud} = \frac{5 \times 10^{-8}}{\langle S \rangle_{cloud}^{3/2}} I^{0.75} \quad \text{Equation 21}$$

471

472 The application of this new correlation, presented in Figure 20 shows an excellent match both for the cumulonimbus and for the simulated stratus. It
 473 remains to be considered whether supersaturation is accessible in the NWP and, if so, if the horizontal resolutions of 1 to 10 km of such models are
 474 sufficiently representative of a real cloud.



475

476 Figure 20. Comparison of the newly-developed correlation Equation 21 with the scavenging modelled by DESCAM for a cumulonimbus and a
477 stratus

478

479

480 3. Conclusions

481

482 The in-cloud scavenging scheme established in this article shows a dependence on rain intensity and average supersaturation in the cloud. Supersaturation
483 allows the scheme to be applicable to both cumulonimbus and stratus clouds. If supersaturation in the cloud is not accessible, it is still possible to apply a
484 different scheme for convective clouds and stratiform clouds. But, since this boundary between the two types of cloud may be ambiguous, it will be
485 preferable to apply the scheme with supersaturation if available.

486 This scavenging scheme is based on the DESCAM microphysical cloud model. This model allows fine-scale description of the life cycle of a cloud up to
487 precipitation development. It tracks particles, crystals, and droplets particle size distributions and models all the water phase changes and, above all, how
488 aerosol particles impact them. The in-cloud scavenging scheme is established by calculating the mass fluxes of particle material exiting the cloud being
489 included in precipitation hydrometeors (both liquid and solid) and based on the mass of particles initially present in the cloud volume.

490 This calculation of cloud volume has proved to be a complex issue, in particular for establishing the altitude of the cloud base, especially when rain occurs.
491 The most relevant method to identify cloud base in this study has been proven to be the one using the number of hydrometeors, rather than the relative
492 humidity or the mass of the hydrometeors. The problem with this method is that this information on the number is not available for most of the NWPs. The
493 use of the in-cloud scavenging scheme must be based on a diagnostic independent of the altitude of the base – and the summit – of the cloud.

494 In the case of stratus cloud, the parametrisation obtained with DESCAM is close to those currently used in the NAME and LdX atmospheric dispersion models,
495 which were established on the basis of the Fukushima accident. As the precipitation that caused deposition of radioactive particles following the accident
496 was largely generated by stratiform clouds, this study confirms *a posteriori* the choice of the in-cloud deposition scheme used to study radioactive deposition
497 following the Fukushima accident and can be extended to all types of cloud.

498 In future works, this deposition scheme will then be used with confidence to study deposition. As an example, it can be used for the deposition of radon
499 progeny (Quérel *et al.*, 2022), in order to statistically measure the impact of this scheme in relation to the existing corpus.

500 Beyond the applications and validations of the scheme described in this article, the scheme itself is currently being refined. First of all, we are working on
501 establishing an in-cloud scavenging rate that will depend on particle size. This important issue was discussed in section 1.3, and requires some modifications
502 to the model to establish a model spectrally. This will make it possible to apply a finer-scale scheme to the atmospheric models with a spectral representation
503 of the particles.

504 The influence of the coefficient κ of the κ -Köhler theory can be also examined. This will make it possible to measure the importance of the physical-chemical
505 properties of the particles: what error is made by applying the same scavenging rate for a hygroscopic aerosol (salt or sulphate) and a non-hygroscopic
506 aerosol (soot, desert dust).

507 The initial particle size distribution of aerosols could also have a significant influence on the final scavenging rate. A distribution centred on 100 nm will not
508 create the same cloud as the same total mass centred around 5 μm particles. This aspect must be assessed.



509 The question of evaporation of droplets between the cloud base and the ground has not yet been addressed. The scheme developed is based on the
510 precipitation intensity at the cloud base, but in the models the precipitation intensity is diagnosed on the ground. This is important for the applicability of
511 the scheme and this difference can lead to errors, especially in the event of high droplet evaporation.

512 Finally, it is not yet established that this scheme is as effective when applied to a model whose spatial resolution is lower than that of DESCAM, as is the
513 case for all Climate (GCM) and Transport (ATM) models.

514 The work still to be carried out will make it possible to best define the scope of validity of this new scheme for in-cloud aerosol scavenging, as well as the
515 uncertainties associated with this model. This will enable the scheme to be used in full knowledge of the facts and according to the highest scientific
516 standards.

517

518

519 **Competing interests**

520 The contact author has declared that none of the authors has any competing interests.

521



522 **References**

- 523 Adachi K, Kajino M, Zaizen Y, Igarashi Y. Emission of spherical cesium-bearing particles from an early stage of the Fukushima nuclear accident. *Sci Rep.*
524 2013;3:2554. doi: 10.1038/srep02554. PMID: 23989894; PMCID: PMC3757362.
- 525 Asai, T., & Kasahara, A. (1967). A theoretical study of the compensating downward motions associated with cumulus clouds. *Journal of Atmospheric*
526 *Sciences*, 24(5), 487-496.
- 527 American Meteorological Society, 2020b: Glossary of meteorology: cloud. Website, accessed on October 21, 2020, URL [http://](http://glossary.ametsoc.org/wiki/cloud)
528 glossary.ametsoc.org/wiki/cloud.
- 529 Baklanov, A., & Sørensen, J. H. (2001). Parameterisation of radionuclide deposition in atmospheric long-range transport modelling. *Physics and Chemistry*
530 *of the Earth, Part B: Hydrology, Oceans and Atmosphere*, 26(10), 787-799.
- 531 Bigg, E. K. (1953). The formation of atmospheric ice crystals by the freezing of droplets. *Quarterly Journal of the Royal Meteorological Society*, 79(342), 510-
532 519.
- 533 Beard, K. V. (1974). Experimental and numerical collision efficiencies for submicron particles scavenged by small raindrops. *Journal of Atmospheric*
534 *Sciences*, 31(6), 1595-1603.
- 535 Bergeron, T. (1928). *Über die dreidimensional verknüpfende Wetteranalyse. 1. Prinzipielle Einführung in das Problem der Luftmassen-und Frontenbildung.*
536 na. Bony, S., & Dufresne, J. L. (2005). Marine boundary layer clouds at the heart of tropical cloud feedback uncertainties in climate models. *Geophysical*
537 *Research Letters*, 32(20).
- 538 Clark, M. J., & Smith, F. B. (1988). Wet and dry deposition of Chernobyl releases. *Nature*, 332(6161), 245-249.
- 539 Costa, M. J., Salgado, R., Santos, D., Levizzani, V., Bortoli, D., Silva, A. M., & Pinto, P. (2010). Modelling of orographic precipitation over Iberia: a springtime
540 case study. *Advances in Geosciences*, 25, 103-110.
- 541 De Cort, M. (1998). Atlas of caesium deposition on Europe after the Chernobyl accident.
- 542 Dépée, A., Lemaître, P., Gelain, T., Mathieu, A., Monier, M., & Flossmann, A. (2019). Theoretical study of aerosol particle electroscavenging by clouds. *Journal*
543 *of Aerosol Science*, 135, 1-20.
- 544 Dépée, A. (2019). *Etude expérimentale et théorique des mécanismes microphysiques mis en jeu dans la capture des aérosols radioactifs par les*
545 *nuages* (Doctoral dissertation, Université Clermont Auvergne [2017-2020]).
- 546 Dépée, A., Lemaître, P., Gelain, T., Monier, M., & Flossmann, A. (2021). Laboratory study of the collection efficiency of submicron aerosol particles by cloud
547 droplets—Part I: Influence of relative humidity. *Atmospheric Chemistry and Physics*, 21(9), 6945-6962.
- 548 Dépée, A., Lemaître, P., Gelain, T., Monier, M., & Flossmann, A. (2021). Laboratory study of the collection efficiency of submicron aerosol particles by cloud
549 droplets—Part II: Influence of electric charges. *Atmospheric Chemistry and Physics*, 21(9), 6963-6984.
- 550 Dye, J. E., Jones, J. J., Winn, W. P., Cerni, T. A., Gardiner, B., Lamb, D., ... & Saunders, C. P. R. (1986). Early electrification and precipitation development in a
551 small, isolated Montana cumulonimbus. *Journal of Geophysical Research: Atmospheres*, 91(D1), 1231-1247.
- 552 Findeisen, Z. (1938). Kolloid meteorologische vorgänge bei neiderschlags-bildung. *Meteorologische Zeitschrift*, 55, 121.
- 553 Flossmann, A. I., Hall, W. D., & Pruppacher, H. R. (1985). A theoretical study of the wet removal of atmospheric pollutants. Part I: The redistribution of aerosol
554 particles captured through nucleation and impaction scavenging by growing cloud drops. *Journal of Atmospheric Sciences*, 42(6), 583-606.
- 555 Flossmann, A. I., Pruppacher, H. R., & Topalian, J. H. (1987). A theoretical study of the wet removal of atmospheric pollutants. Part II: The uptake and
556 redistribution of (NH₄)₂SO₄ particles and SO₂ gas simultaneously scavenged by growing cloud drops. *Journal of Atmospheric Sciences*, 44(20), 2912-2923.
- 557 Flossmann, A. I., & Pruppacher, H. R. (1988). A theoretical study of the wet removal of atmospheric pollutants. Part III: The uptake, redistribution, and
558 deposition of (NH₄)₂SO₄ particles by a convective cloud using a two-dimensional cloud dynamics model. *Journal of Atmospheric Sciences*, 45(13), 1857-
559 1871.
- 560 Flossmann, A. I. (1998). Clouds and pollution. *Pure and applied chemistry*, 70(7), 1345-1352.
- 561 Flossmann, A. I., & Wobrock, W. (2010). A review of our understanding of the aerosol–cloud interaction from the perspective of a bin resolved cloud scale
562 modelling. *Atmospheric Research*, 97(4), 478-497.
- 563 Groëll, J., Quélo, D., & Mathieu, A. (2014). Sensitivity analysis of the modelled deposition of 137 Cs on the Japanese land following the Fukushima
564 accident. *International Journal of Environment and Pollution*, 55(1-4), 67-75.



- 565 Hertel, O., Christensen, J., Runge, E. H., Asman, W. A., Berkowicz, R., Hovmand, M. F., & Hov, Ø. (1995). Development and testing of a new variable scale air
566 pollution model—ACDEP. *Atmospheric Environment*, 29(11), 1267-1290.
- 567 Hirsch, E., Koren, I., Levin, Z., Altaratz, O., & Agassi, E. (2014). On transition-zone water clouds. *Atmospheric Chemistry and Physics*, 14(17), 9001-9012.
- 568 Hiron, T., & Flossmann, A. I. (2015). A study of the role of the parameterization of heterogeneous ice nucleation for the modeling of microphysics and
569 precipitation of a convective cloud. *Journal of the Atmospheric Sciences*, 72(9), 3322-3339.
- 570 Hiron, T. (2017). *Experimental and modeling study of heterogeneous ice nucleation on mineral aerosol particles and its impact on a convective cloud* (Doctoral
571 dissertation, Université Clermont Auvergne).
- 572 Kerker, M., & Hampl, V. (1974). Scavenging of Aerosol Particles by a Falling Water Drop and Calculation of Washout Coefficients. *Journal of Atmospheric*
573 *Sciences*, 31(5), 1368-1376.
- 574 Kinoshita, N., Sueki, K., Sasa, K., Kitagawa, J. I., Ikarashi, S., Nishimura, T., ... & Yamagata, T. (2011). Assessment of individual radionuclide distributions from
575 the Fukushima nuclear accident covering central-east Japan. *Proceedings of the National Academy of Sciences*, 108(49), 19526-19529.
- 576 Klein, É. (2021). *Les tactiques de Chronos*. Flammarion.
- 577 Klein, É. (2019). *Ce qui est sans être tout à fait: essai sur le vide*. Éditions Actes Sud.
- 578 Knight, C. A. (1982). The cooperative convective precipitation experiment (CCOPE), 18 May–7 August 1981. *Bulletin of the American Meteorological*
579 *Society*, 63(4), 386-398.
- 580 Koop, T., Luo, B., Tsias, A., & Peter, T. (2000). Water activity as the determinant for homogeneous ice nucleation in aqueous solutions. *Nature*, 406(6796),
581 611-614.
- 582 Lai, K. Y., Dayan, N., & Kerker, M. (1978). Scavenging of aerosol particles by a falling water drop. *Journal of Atmospheric Sciences*, 35(4), 674-682.
- 583 Leadbetter, S. J., Hort, M. C., Jones, A. R., Webster, H. N., & Draxler, R. R. (2015). Sensitivity of the modelled deposition of Caesium-137 from the Fukushima
584 Dai-ichi nuclear power plant to the wet deposition parameterisation in NAME. *Journal of environmental radioactivity*, 139, 200-211.
- 585 Leaitch, W., Strapp, J. W., Isaac, G. A., & Hudson, J. G. (1986). Cloud droplet nucleation and cloud scavenging of aerosol sulphate in polluted
586 atmospheres. *Tellus B: Chemical and Physical Meteorology*, 38(5), 328-344.
- 587 Lemaitre, P., Querel, A., Monier, M., Menard, T., Porcheron, E., & Flossmann, A. I. (2017). Experimental evidence of the rear capture of aerosol particles by
588 raindrops. *Atmospheric Chemistry and Physics*, 17(6), 4159-4176.
- 589 Leroy, D., Monier, M., Wobrock, W., & Flossmann, A. I. (2006). A numerical study of the effects of the aerosol particle spectrum on the development of the
590 ice phase and precipitation formation. *Atmospheric Research*, 80(1), 15-45.
- 591 Leroy, D., Wobrock, W., & Flossmann, A. I. (2007). On the influence of the treatment of aerosol particles in different bin microphysical models: a comparison
592 between two different schemes. *Atmospheric research*, 85(3-4), 269-287.
- 593 Meyers, M. P., DeMott, P. J., & Cotton, W. R. (1992). New primary ice-nucleation parameterizations in an explicit cloud model. *Journal of Applied Meteorology*
594 *and Climatology*, 31(7), 708-721.
- 595 Monier, M., Wobrock, W., Gayet, J.-F., Flossmann, A., (2006). Development of a detailed microphysics cirrus model for interpretation of the recent INCA
596 campaign. *J. Atmos. Sci.* 163.
- 597 Mathieu, A., Korsakissok, I., Quélo, D., Groëll, J., Tombette, M., Didier, D., ... & Isnard, O. (2012). Atmospheric dispersion and deposition of radionuclides
598 from the Fukushima Daiichi nuclear power plant accident. *Elements*, 8(3), 195-200.
- 599 MRI, 2015. JMA-RATM Technical Report, vol. 76.
- 600 Palmer, T. (2014). Climate forecasting: Build high-resolution global climate models. *Nature*, 515(7527), 338-339.
- 601 Petters, M. D., & Kreidenweis, S. M. (2007). A single parameter representation of hygroscopic growth and cloud condensation nucleus activity. *Atmospheric*
602 *Chemistry and Physics*, 7(8), 1961-1971.
- 603 Petroff, A., Mailliat, A., Amielh, M., & Anselmet, F. (2008). Aerosol dry deposition on vegetative canopies. Part I: review of present knowledge. *Atmospheric*
604 *Environment*, 42(16), 3625-3653.
- 605 Pranesha, T. S., & Kamra, A. K. (1996). Scavenging of aerosol particles by large water drops: 1. Neutral case. *Journal of Geophysical Research:*
606 *Atmospheres*, 101(D18), 23373-23380.



- 607 Pruppacher, H. R., Klett, J. D., & Wang, P. K. (1998). *Microphysics of clouds and precipitation*. 2nd ed., Atmospheric and Oceanographic Sciences Library,
608 Kluwer Academic Publishers, doi:10.1080/02786829808965531.
- 609 Quélo, D., Krysta, M., Bocquet, M., Isnard, O., Minier, Y., & Sportisse, B. (2007). Validation of the Polyphemus platform on the ETEX, Chernobyl and Algeciras
610 cases. *Atmospheric environment*, 41(26), 5300-5315.
- 611 Quérel, A., Monier, M., Flossmann, A. I., Lemaitre, P., & Porcheron, E. (2014). The importance of new collection efficiency values including the effect of rear
612 capture for the below-cloud scavenging of aerosol particles. *Atmospheric research*, 142, 57-66.
- 613 Quérel, A., Quelo, D., Roustan, Y., & Mathieu, A. (2021). Sensitivity study to select the wet deposition scheme in an operational atmospheric transport
614 model. *Journal of Environmental Radioactivity*, 237, 106712.
- 615 Quérel, A., Meddouni, K., Quélo, D., Doursout, T., Chuzel, S., 2022. Statistical approach to assess radon-222 long-range atmospheric transport modelling and
616 its associated gamma dose rate peaks, in: *Advances in Geosciences*. Presented at the Geoscience applications of environmental radioactivity - EGU General
617 Assembly 2021, Online, 19–30 April 2021, Copernicus GmbH, pp. 109–124.
- 618 Saito, K., Shimbori, T., & Draxler, R. (2015). JMA's regional atmospheric transport model calculations for the WMO technical task team on meteorological
619 analyses for Fukushima Daiichi Nuclear Power Plant accident. *Journal of environmental radioactivity*, 139, 185-199.
- 620 Sassen, K., and B. S. Cho, 1992: Subvisual-thin cirrus lidar dataset for satellite verification and climatological research. *J. Appl. Meteorol.*, 31, 1275–1285,
621 doi:10.1175/1520-0450(1992)031<1275:STCLDF>2.0.CO;2, https://doi.org/10.1175/1520-0450(1992)031<1275:STCLDF>
622 2.0.CO;2.
- 623 Saito, K., Shimbori, T., & Draxler, R. (2015). JMA's regional atmospheric transport model calculations for the WMO technical task team on meteorological
624 analyses for Fukushima Daiichi Nuclear Power Plant accident. *Journal of environmental radioactivity*, 139, 185-199.
- 625 Sievering, H., Van Valin, C. C., Barrett, E. W., & Pueschel, R. F. (1984). Cloud scavenging of aerosol sulfur: Two case studies. *Atmospheric Environment*
626 (1967), 18(12), 2685-2690.
- 627 Slinn, W. G. N.: Some approximations for the wet and dry removal of particles and gases from the atmosphere, *Water Air Soil Poll.*, 7, 513–543, 1977.
- 628 Spänkuch, D., Hellmuth, O., & Görtdorf, U. (2022). What is a cloud? Toward a more precise definition?. *Bulletin of the American Meteorological Society*.
- 629 Stephan, K., Klink, S., & Schraff, C. (2008). Assimilation of radar-derived rain rates into the convective-scale model COSMO-DE at DWD. *Quarterly Journal of*
630 *the Royal Meteorological Society: A journal of the atmospheric sciences, applied meteorology and physical oceanography*, 134(634), 1315-1326.
- 631 Wegener, A. (1911). *Thermodynamik der Atmosphäre*. JA Barth.
- 632 Vali, G., DeMott, P. J., Möhler, O., & Whale, T. F. (2015). A proposal for ice nucleation terminology. *Atmospheric Chemistry and Physics*, 15(18), 10263-10270.
- 633 Vohl, O., Mitra, S. K., Wurzler, S. C., & Pruppacher, H. R. (1999). A wind tunnel study of the effects of turbulence on the growth of cloud drops by collision
634 and coalescence. *Journal of the atmospheric sciences*, 56(24), 4088-4099.
- 635 Wang, H., & Su, W. (2013). Evaluating and understanding top of the atmosphere cloud radiative effects in Intergovernmental Panel on Climate Change (IPCC)
636 Fifth Assessment Report (AR5) Coupled Model Intercomparison Project Phase 5 (CMIP5) models using satellite observations. *Journal of Geophysical*
637 *Research: Atmospheres*, 118(2), 683-699.
- 638 WMO. (2014). *Guide to Meteorological Instruments and Methods of Observation (CIMO Guide, WMO-No. 8*. Wood, R., & Field, P. R. (2011). The distribution
639 of cloud horizontal sizes. *Journal of Climate*, 24 (18), 4800-4816.
- 640 Zhang, L., Michelangeli, D. V., & Taylor, P. A. (2004). Numerical studies of aerosol scavenging by low-level, warm stratiform clouds and
641 precipitation. *Atmospheric Environment*, 38(28), 4653-4665.
- 642 Zhang, S., Xiang, M., Xu, Z., Wang, L., & Zhang, C. (2020). Evaluation of water cycle health status based on a cloud model. *Journal of cleaner production*, 245,
643 118850.
- 644